



# Flow Separation Control of an Ultra-compact S-shaped Convergent-divergent Nozzle Using the Blowing Method

J. W. Shi, Z. H. Hui<sup>†</sup>, L. Zhou and Z. X. Wang

*School of Power and Energy, Northwestern Polytechnical University, Xi'an, Shaan Xi Province, 710072, China*

<sup>†</sup>Corresponding Author Email: [huizh36@mail.nwpu.edu.cn](mailto:huizh36@mail.nwpu.edu.cn)

## ABSTRACT

To enhance the aerodynamic performance of an ultra-compact S-shaped convergent-divergent nozzle and mitigate flow separation, numerical simulations were conducted using FLUENT software. The study employed the  $k-\omega$  shear stress transport turbulent model to investigate a flow control method involving blowing. Detailed analysis was performed on the impact of blowing position, angle, and pressure ratio on controlling flow separation. The findings indicate that as the blowing position moves backward, the flow separation area diminishes. Additionally, downstream flow separation ceases at smaller blowing angles within the separation zone. However, excessively large blowing angles tend to create an “aerodynamic wall,” causing significant upstream flow loss and nozzle performance degradation. Enhancing the blowing pressure ratio, given proper mixing with low-energy fluid and no interference with the main flow, can improve the nozzle's aerodynamic performance. Under the optimal blowing scheme, the total pressure recovery coefficient and thrust coefficient are increased by approximately 0.52% and 3.75%, respectively, when compared with those of the reference nozzle.

## Article History

Received October 25, 2023  
Revised December 28, 2023  
Accepted January 16, 2024  
Available online March 27, 2024

## Keywords:

*S-shaped nozzle  
Flow separation  
Blowing control method  
Flow control  
Numerical simulation*

## 1. INTRODUCTION

The radiation emitted from aircraft engine exhaust systems significantly impacts aircraft stealth capabilities. S-shaped nozzles effectively shield internal high-temperature components, swiftly reducing infrared and electromagnetic radiation (Song et al., 2010; Sun et al., 2011). Consequently, these nozzles find application in B-2A “Ghost” strategic bombers, X-45A unmanned fighter jets, French “Neuron” unmanned aerial vehicles (UAVs), and other aircraft (Wise, 2003; Xu et al., 2012). To ensure fighter jets' superior maneuverability and broader flight envelope of the fighter jets, the axial length of the S-shaped nozzle should be reduced, and the convergent-divergent configuration should be adopted to the design of the exhaust system. Therefore, the ultra-compact S-shaped convergent-divergent nozzle with reduced axial length and a convergent-divergent configuration is preferred. However, the nozzle's considerable offset and sharp turns compromise its aerodynamic performance, leading to internal flow separation. Hence, it becomes imperative to implement control measures for the internal flow of the ultra-compact S-shaped convergent-divergent nozzle to enhance its aerodynamic efficiency.

In the research regarding S-shaped convergent-divergent nozzles, Crowe & Martin (2015, 2019) investigated the impact of aspect ratio and inlet pre-swirl on aerodynamic parameters and temperature distribution at the nozzle outlet. Their findings indicated that increasing the aspect ratio enhances the flow coefficient without significantly affecting the thrust coefficient. Improved nozzle performance was observed with higher aspect ratios, which helped avoid flow separation when the aspect ratio exceeded 3. Additionally, a slight pre-swirl enhanced temperature uniformity. However, their study focused on conventional S-shaped convergent-divergent nozzles, and their conclusions may not be applicable to ultra-compact variants of these nozzles. Zhou et al. (2021) explored the influence of nozzle pressure ratio and outlet area ratio on the flow characteristics of S-shaped convergent-divergent nozzles. Results highlighted how pressure ratio affected separation distribution and shock wave position in the tube. At specific outlet area ratios, flow separation occurred on the upper wall of the first curved pipe, substantially reducing the nozzle's aerodynamic performance. Unfortunately, this study merely observed flow separation phenomena without proposing control measures. Wang et al. (2018) delved into the flow mechanism of ultra-compact S-shaped

NOMENCLATURE			
$a$	length of blowing device	$P_0$	ambient pressure
$A_8$	nozzle throat area	$P^*$	total pressure of nozzle inlet
$A_9$	nozzle exit area	$T_0$	ambient temperature
$b$	width of blowing device	$T^*$	total temperature of nozzle inlet
$BPR$	Blowing Pressure Ratio	$W/H$	aspect ratio on nozzle exit plane
$C_{fg}$	thrust coefficient	$\alpha$	angle of attack
$D$	inlet diameter of the nozzle	$x/L$	dimensionless longitudinal blowing position
$L$	length of serpentine nozzle	$y^+$	dimensionless height of the first lay grid
$Ma$	Mach number	$z/L$	dimensionless span-wise blowing position
$Ma_\infty$	Mach number of free stream	$\sigma$	total pressure recovery coefficient
$NPR$	Nozzle Pressure Ratio	$\theta$	blowing angle

convergent-divergent nozzles, employing suction flow control to mitigate flow separation in the field (Wang et al., 2018). Their results indicated that initiating suction control before the separation zone helped alleviate the separation, markedly enhancing the nozzle's aerodynamic performance. However, this method did not completely resolve flow separation and presented challenges for implementation in confined spaces. Consequently, despite various studies, internal separation issues persist in ultra-compact S-shaped convergent-divergent nozzles as large deflection and sharp turns, resulting in obvious flow separation inside. The aerodynamic performance of the nozzle experiences a sharp decline, with internal separation persisting despite existing research efforts. To enhance this performance, alternative flow control methods must be explored.

Limited literature exists on flow control techniques for S-shaped nozzles. Given the similarity between the configurations of S-shaped nozzles and S-shaped inlets, insights from the latter can serve as a reliable reference for the S-shaped nozzle. Initial research on S-shaped inlet flow control began in the 1980s, primarily employing vortex generators as the control method. Vakili and Kunik investigated the impact of vortex generators on inlet performance using experimental and numerical simulation methods (Vakili et al., 1985; Kunik 1986). Their findings revealed the disappearance of flow separation within the inlet post-control, notably reducing outlet distortion. However, this approach adversely affected nozzle aerodynamics and increased structural complexity. Advancements in flow control theory and technology led to exploration of mainstream methods, including boundary layer blowing and suction, synthetic jet, and jet vortex generator, for S-shaped inlet control (Vikas & Farrukh, 2003; Jing and Guo, 2007; Sang, 2010; Zhao et al., 2010, 2011; Chen & Wang 2012; He & Dong 2015; Liu 2015). The results indicated that blowing and suction methods effectively improved flow field quality while significantly enhancing inlet aerodynamics with minimal secondary flow consumption. However, the flow conditions in S-shaped nozzles differ significantly from S-shaped inlets due to higher velocities, intricate pressure gradients, and vortex systems. Hence, the flow control principles for S-shaped nozzles substantially vary from those of S-shaped inlets. Sankar et al. (2016, 2017, 2018, Reddy and Sankar (2020), and Swamy et al. (2022) conducted comprehensive numerical investigations on thermal transport and fluid flow characteristics in the

annular space, providing valuable insights into implementing flow control in ultra-compact S-shaped convergent-divergent nozzles. Although blowing and suction control methods effectively alleviate separation in S-shaped inlets, applying these methods to S-shaped nozzles poses significant challenges due to intricate vortex systems, unique flow phenomena, and energy losses in the serpentine nozzle.

This literature survey highlights ultra-compact S-shaped convergent-divergent nozzles as an optimal choice for fighter jets boasting super maneuverability and expanded flight capabilities. Nevertheless, these nozzles exhibit complex flow traits, leading to pronounced separation due to their ultra-compact configuration. As a result, controlling flow separation in ultra-compact S-shaped convergent-divergent nozzles differs not only from the approaches described in existing literature but also from conventional S-shaped counterparts. Consequently, this study aims to employ blowing control methods for the ultra-compact S-shaped convergent-divergent nozzle to address flow separation issues. Numerical simulations, utilizing CFD software with the  $k-\omega$  shear stress transport (SST) turbulent model, were conducted to investigate the blowing flow control method. The study delves into the effects of blowing method position, angle, and pressure ratio, aiming to establish a foundation for designing high-performance ultra-compact S-shaped convergent-divergent nozzles.

## 2. GEOMETRIC MODEL AND NUMERICAL METHODOLOGY

### 2.1 Geometric Model

The geometrical configuration of the ultra-compact S-shaped convergent-divergent nozzle, equipped with a blowing device, as discussed in this study, is illustrated in Fig. 1. The nozzle's inlet diameter ( $D$ ) measures 871.4 mm, with a length ( $L$ ) of 1913.9 mm. Its length-to-diameter ratio is 2.2, and the ratio of nozzle exit area to the nozzle throat area ( $A_9/A_8$ ) is 1.37. Additionally, the outlet aspect ratio ( $W/H$ ) is 3.86. The blowing device comprises a rectangular blowing groove measuring  $0.593D \times 0.022D$ . Figure 2 demonstrates the positioning of the blowing device using relative coordinates  $x/L$ , specified as 0.26, 0.28, and 0.30, located respectively in the front, middle front, and within the separation zone. The blowing angle (the angle between the center line of the blowing slot and

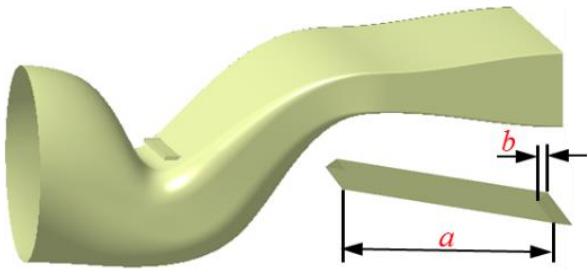


**Fig. 1 Geometric model**

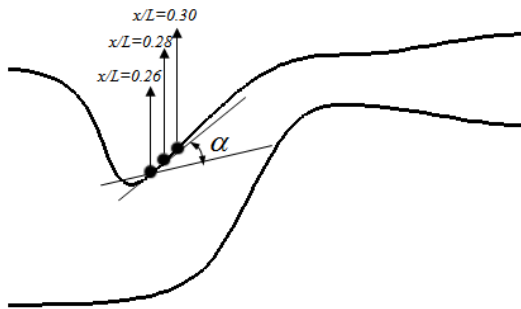
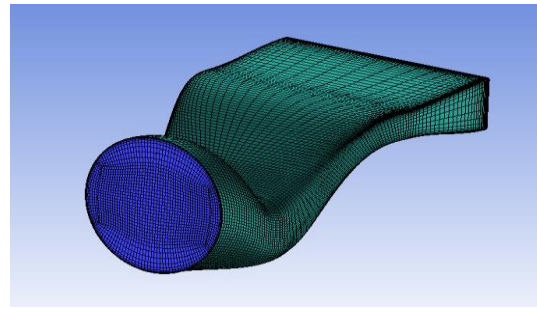
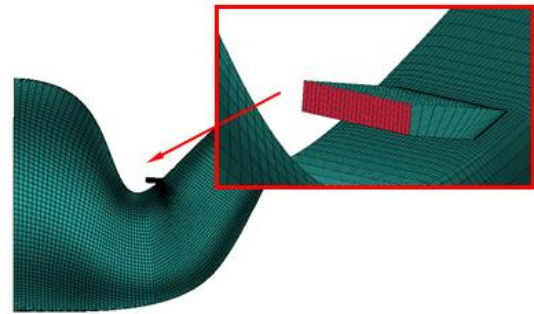


**Fig. 2 Arrangement position and angle of blowing**



(a) Mesh on the inlet and the wall of the nozzle



(b) Mesh on the outlet and the wall of blowing

**Fig. 3 Computational grid**

the tangent direction of the blowing point) ranges from 20° to 90°, with increments of 15° (20°, 30°, 45°, 60°, 75°, and 90°).

## 2.2 Numerical Methodology

Structured grids generated using ICEM software are employed in all computations. Mesh refinement near the wall ensures proper resolution of the wall ( $y^+ < 1$ ). The total grid count amounts to 1.6 million. Figure 3 displays the grid distribution for the inlet and wall of the nozzle, as well as the outlet and wall of the blowing section. FLUENT software, utilizing a density-coupled solver, resolves the Reynolds-averaged Navier–Stokes equations employing the SST  $\kappa$ - $\omega$  turbulence model. Central difference schemes handle spatial discretization of viscous terms in all equations, while a fully implicit form manages the time term.

## 2.3 Boundary Conditions

For the flow field, far-field boundary conditions are set with a uniform Mach number  $Ma_\infty = 0.05$ ,  $P_0 = 101.3$  kPa for static pressure, and a specified static temperature  $T_0 = 300$  K. The inflow direction aligns parallel to the nozzle's inlet axis. Although the far-field inlet Mach number  $Ma_\infty = 0$ , for computational convergence of calculations,  $Ma_\infty$  is adjusted to 0.05.

Subsonic inlet boundary conditions incorporating uniform total pressure and total temperature are applied to the nozzle and the blowing duct inlets. For the nozzle inlet,  $P^* = 904.3$  kPa  $T^* = 800$  K is set. Different secondary flow total pressures are designated for the blowing secondary flow inlet, based on the blowing pressure ratio (BPR; defined as the ratio of blowing flow total pressure to nozzle flow total pressure), varying at 0.7, 0.8, 0.9, and 1.0, respectively.

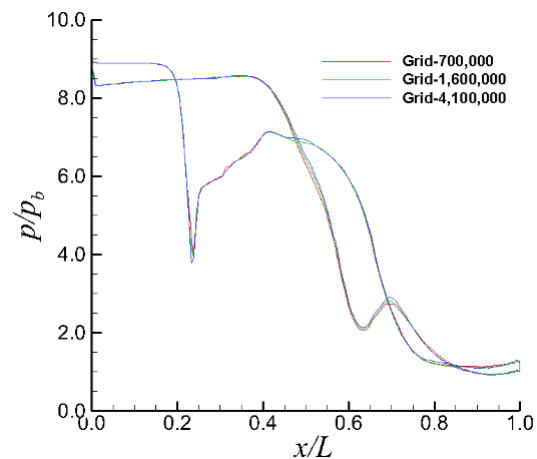


**Fig. 4 Comparison of static pressure distribution on the upper and lower walls of the nozzle symmetry plane under different grid sizes**

## 2.4 Grid Independence

To ensure grid independence and minimize its influence on the simulation results, a grid independence check is conducted. The flow field characteristics are computed for three different grid sizes: 0.7 million, 1.6 million, and 4.1 million. Figure 4 illustrates the comparison of static pressure distribution under varying grid counts. The pressure distributions for these three grid sizes are nearly identical. Although slight differences are observed with 0.7 million grids, the maximum relative error is 2.2%. Consequently, 1.6 million grids are utilized in this study.

### 2.5 Validation of the CFD Method

The flow fields within the ultra-compact S-shaped convergent-divergent nozzle were derived by solving the Reynolds-averaged Navier–Stokes equations using the SST  $\kappa\text{-}\omega$  turbulence model. To verify the accuracy of the numerical method, calculations were performed based on the experimental model of a convergent serpentine nozzle from Hui et al. (2021). Detailed descriptions of their experimental setup, geometric parameters, and boundary conditions are available in the referenced work. For this validation, the applied boundary conditions were: a core flow pressure ratio of 3, a bypass flow pressure ratio of 3. Comparison results, depicted in Fig. 5, indicate that the  $\kappa\text{-}\omega$  SST turbulent model accurately predicts the flow characteristics of the serpentine nozzle. Similarly, Sun et al. (2014) validated their numerical method, also affirming that the  $\kappa\text{-}\omega$  SST turbulent model reliably predicts the static pressure distribution on the wall of the serpentine nozzle.

To further affirm the accuracy of the aforementioned numerical method in obtaining precise flow field information within the S-shaped convergent-divergent nozzle, an experiment using this nozzle was conducted at the dual flow exhaust system test facility. This facility is equipped with flow control devices, pressure control devices, force measurement devices, and various flow field measurement instruments, including the PSI pressure scanning valve (with a precision of within 0.05%) and a schlieren system. The experimental model, depicted in Fig. 6, is a scaled-down version of Fig. 1, with a scaling factor of 11. The validation experiment was carried out under a condition of nozzle pressure ratio (NPR) of 2.2. The pressure distributions on the nozzle walls were measured and are illustrated in Fig. 7. Under this experimental condition, flow separation occurred in the nozzle divergent section due to over-expansion of the main flow. The results demonstrate that the CFD method effectively predicts the nozzle wall pressure distributions and flow separation position, consistent with experimental data, with a maximum error within 2%. Thus, it is concluded that the numerical scheme employed in this study is efficient.

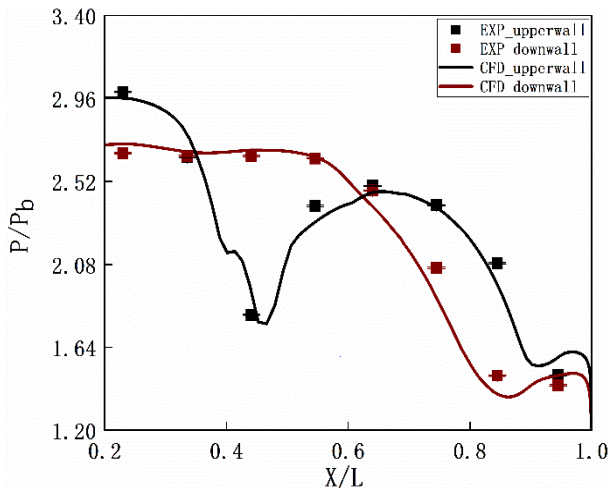


Fig. 5 Comparison of static pressure

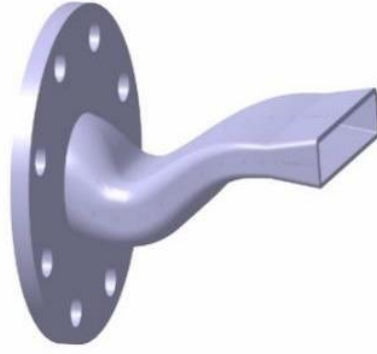


Fig. 6 Experimental model for CFD validation

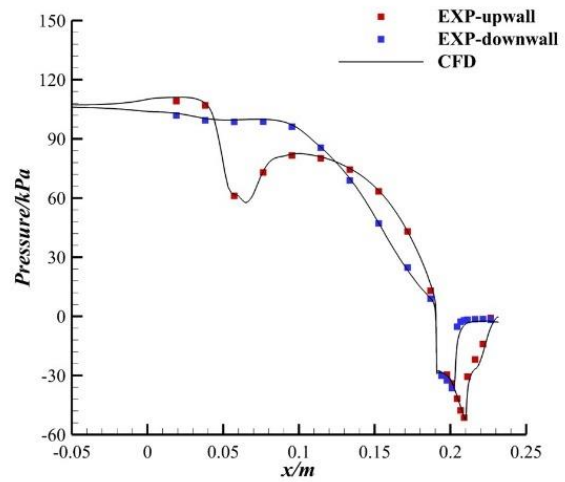


Fig. 7 Comparison between experimental data and CFD results (on the top wall and bottom wall)

### 2.6 Definition of Parameters

The total pressure recovery coefficient  $\sigma$ , mass flow coefficient  $C_D$ , and thrust coefficient  $C_{fg}$  are used to evaluate the aerodynamic performance of the ultra-compact S-shaped convergent-divergent nozzle.

The total pressure recovery coefficient is expressed as

$$\sigma = \frac{P_2^*}{P_1^*}, \quad (1)$$

where  $P_2^*$  is the total pressure of the nozzle outlet, and  $P_1^*$  is the total pressure of the nozzle inlet. The mass flow coefficient  $C_D$  is expressed as

$$C_D = \frac{G_1}{m_1 + m_2}, \quad (2)$$

where  $G_1$  represents the actual mass flow rate at the nozzle outlet,  $m_1$  and  $m_2$  represent the ideal mass flow rate of the mainstream and blowing flow, respectively. The thrust coefficient  $C_{fg}$  is expressed as

$$C_{fg} = \frac{\int \rho v_x^2 + (p - 101325) dA}{C_1 \times G_1 + C_2 \times G_2}, \quad (3)$$

where  $C_1$  and  $C_2$  represent the ideal velocity of the mainstream and blowing flow, respectively;  $G_1$  and  $G_2$

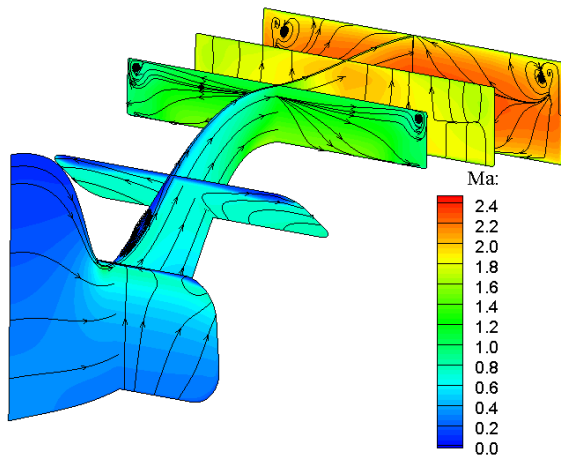


**Fig. 8** Distribution of Ma number and streamline at different longitudinal sections of the nozzle

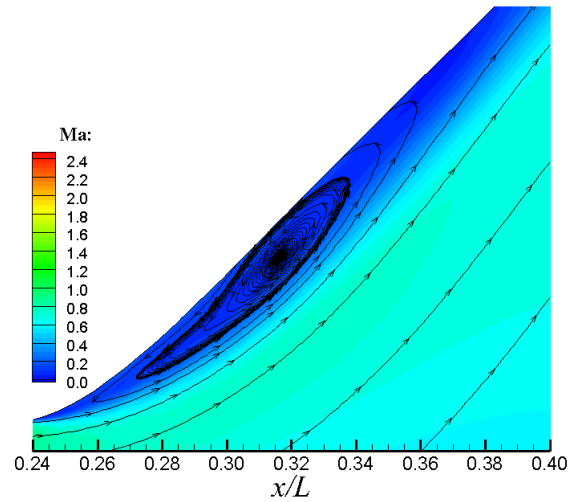


**Fig. 9** Flow separation on the symmetric plane

represent the actual mass flow rate of the mainstream and blowing flow, respectively;  $v_x$  represents the velocity component in the X direction at the nozzle outlet.

The NPR represents the ratio of the total pressure of the nozzle inlet to ambient pressure. The NPR is expressed as

$$NPR = P_1^*/P_0 \quad (4)$$

BPR represents the ratio of total pressure of the blowing flow inlet to total pressure of the nozzle inlet. The blowing flow pressure ratio can be expressed as

$$BPR = P_3^*/P_1^* \quad (5)$$

### 3. RESULTS AND ANALYSIS

#### 3.1 Analysis of the Reference Nozzle

To explore the impact of blowing control on the flow field and aerodynamic performance of the nozzle, a numerical investigation was initially conducted on the reference nozzle without the blowing device at a designed NPR of 8.925. As shown in Fig. 8. The airflow accelerates within the nozzle, exhibiting significant non-uniformity in Mach number distribution across flow sections. Notably, transverse flow is evident inside the nozzle, with local acceleration zones observed at the upper wall of the first bend and the lower wall of the second bend. As the airflow traverses the two turns in the S-shaped nozzle, a separation vortex emerges downstream of the first turn. Figure 9 presents a detailed view of the separation zone, attributed to the sharp turn and significant offset after the first turn of the nozzle, and the fluid near the wall is subjected to large centrifugal force; therefore, the flow separation is formed under the local adverse pressure gradients downstream. Examining the shear stress distribution of the nozzle wall in Fig. 10, it is evident that the wall's limit streamline converges into a line at the upper wall of the first turn, indicating low-energy fluid flow recirculation upstream along the upper wall of the nozzle.

The presented results highlight the induction of flow separation in the ultra-compact S-shaped convergent-divergent nozzle due to its compact design and significant

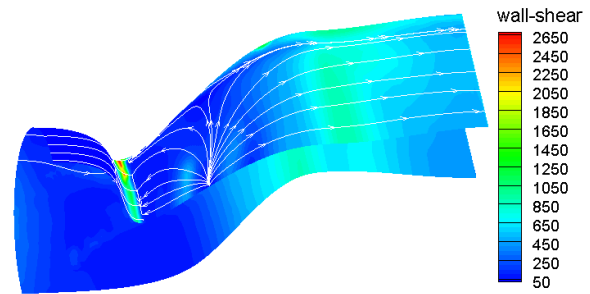


**Fig. 10** Limited streamline of the nozzle wall

offset, significantly influencing the nozzle's aerodynamic performance. The thrust coefficient ( $C_{fg}$ ) and total pressure recovery coefficient  $\sigma$  register notably low values at 0.9546 and 0.9577, respectively. Hence, implementing flow control measures becomes imperative to enhance its performance.

#### 3.2 Results and Discussion

##### 3.2.1 Effect of Blowing Position

The method of blowing flow control involves injecting high-energy fluid into the boundary layer to enhance the capability of low-energy fluid in overcoming adverse pressure gradients. Analyzing the nozzle under design conditions with a BPR set at BPR=1, the impact of axial blowing position on blowing effectiveness is investigated at various blowing angles. Figure 11 depicts alterations in nozzle outlet flow coefficient, total pressure recovery coefficient, and thrust coefficient concerning blowing angles at different blowing positions.

The aerodynamic parameters of the nozzle demonstrate improvement with a backward shift in the blowing position. While the trends vary at different angles (e.g., at a 20° blowing angle, the aerodynamic performance initially increases then decreases, whereas at a 75° blowing angle, it gradually improves), overall, the blowing control proves more effective in the separation zone (specifically at  $x/L=0.28$  and  $x/L=0.30$ ) than that before the separation zone (i.e.,  $x/L=0.26$ ). This control method injects energy into the low-energy fluid within the

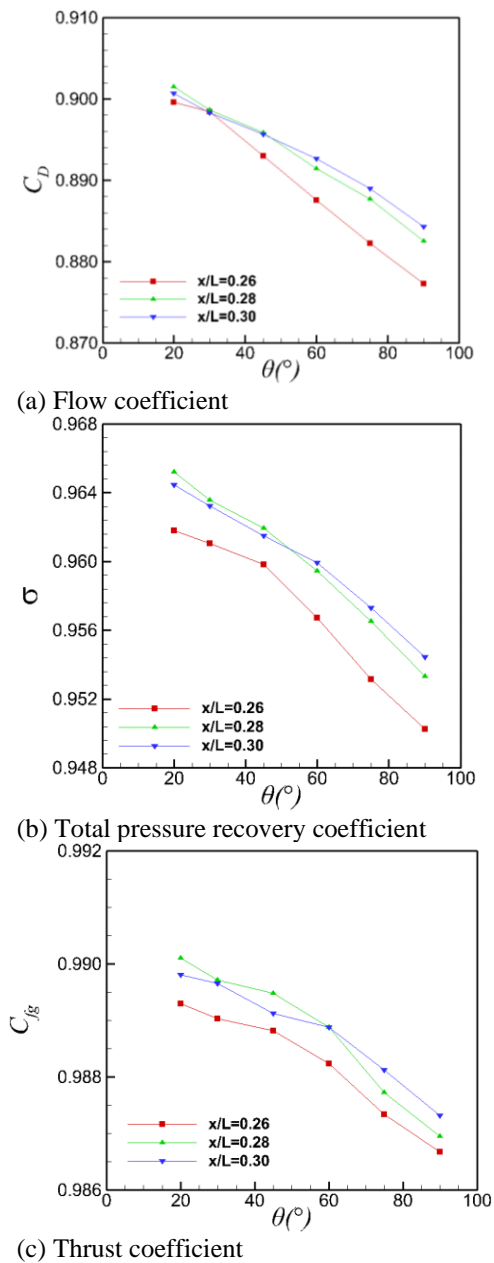


**Fig. 11** Variation in aerodynamic performance parameters with blowing angle under different blowing positions

boundary layer, enhancing its ability to counteract adverse pressure gradients. However, because of the limitation of geometric configuration, ensuring alignment between the secondary flow direction and the nozzle flow is not feasible. Consequently, only a portion of the high-energy fluid's energy is absorbed by the low-energy fluid in the boundary layer. When the blowing device is positioned ahead of the separation zone, the incomplete separation development and thin boundary layer result in less mixing between the secondary flow and low-energy fluid. Moreover, the distant blowing flow from the separation center easily leads to renewed wall-adjacent low-energy fluid separation under adverse pressure gradients. Placing the blowing position nearer to the separation zone's middle/front ( $x/L=0.28$ ) results in fully developed separation and thicker boundary layers, facilitating increased mixing and enhanced capability to counter

adverse pressure gradients, thus yielding better blowing effects compared to pre-separation zone positions. When the blowing position is behind the separation zone, the nozzle's performance remains largely unchanged.

In Fig. 12, the Ma number and streamline distribution exhibit variations at different axial positions when the BPR equals 1 at 20° and 75° blowing angles. Blowing control at different axial positions has different effects on the flow field downstream and upstream of the blowing position. Backward movement of the blowing position gradually reduces the downstream separation zone while increasing the separation zone upstream. This trend is consistent across various angles due to the secondary flow injection, creating a certain jet depth. This “pneumatic wall” effect blocks the movement of upstream low-energy fluid. Therefore, the separation zone upstream of the blowing port still exists and increases with the backward movement of the blowing port. For the downstream low-energy fluid, the secondary flow as a high-energy fluid is a supplement to energy. The more backward the blowing position is, the stronger the mixing of the downstream low-energy fluid is, and the thinner the downstream separation zone is. Compared with the separation zone upstream of the blowing position, the development of downstream flow separation has a greater effect on the aerodynamic performance of the nozzle, making blowing control more effective in the separation zone compared to pre-separation.

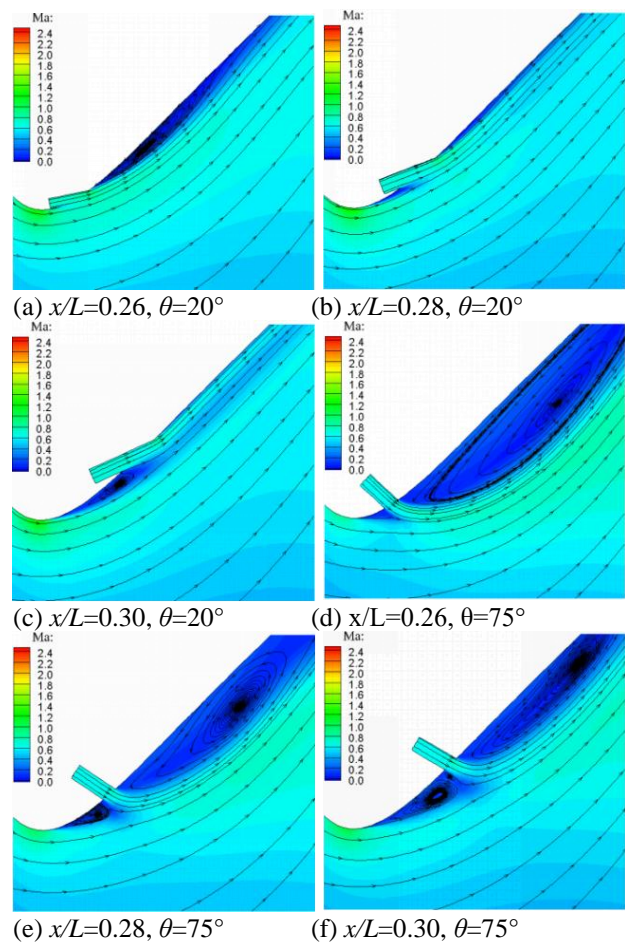


**Fig. 12** Distribution of Ma number and streamlines at different angles and local positions

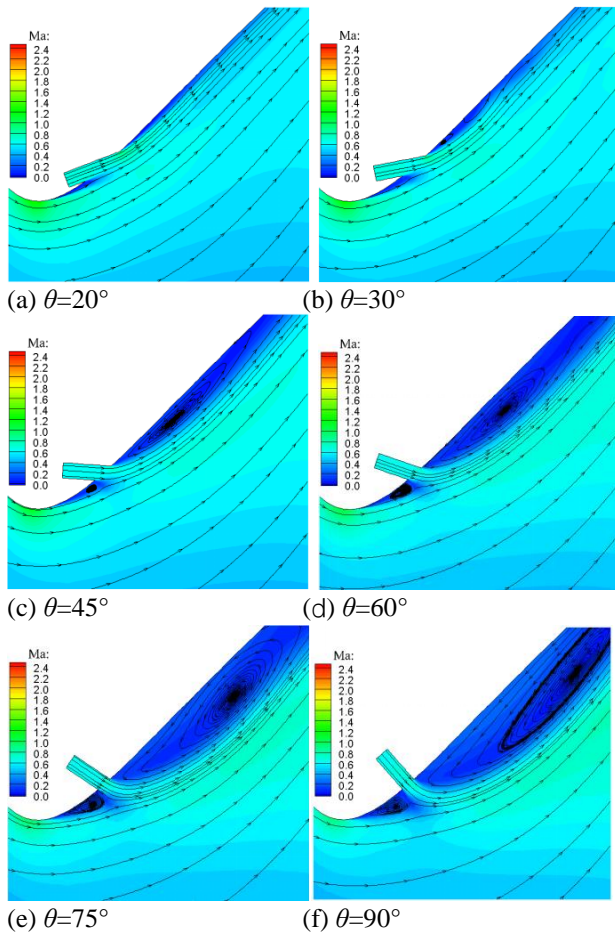


**Fig. 13 Distribution of Ma number and streamline of the symmetry plane at  $x/L=0.28$**

### 3.2.2 Effect of Blowing Angle

The influence of angle on blowing effect is evident (Fig. 11). The flow coefficient, total pressure recovery coefficient, and thrust coefficient decrease with increased blowing angles under constant BPR conditions. This trend persists across various blowing positions due to secondary flow mixing with nozzle airflow. A smaller blowing angle injects more flow into the boundary layer, while a larger angle decreases boundary layer injection but increases flow blown into the nozzle, elevating total pressure loss and reducing the outlet's total pressure recovery coefficient. Under the same position pressure ratio of the blowing, the jet depth of the secondary flow remains the same. As blowing angle increases, the secondary flow's normal jet depth in the nozzle's mainstream direction rises, intensifying aerodynamic blockage upstream of the blowing position, decreasing nozzle flow capacity, flow coefficient, and thrust coefficient at the outlet.

Figure 13 illustrates the distributions of Ma number and streamline on the symmetry plane at  $x/L=0.28$ , which is ahead of the separation zone, for various blowing angles. Observably, both the downstream and upstream separation zones from the blowing position tend to enlarge with higher blowing angles. At  $20^\circ$  and  $30^\circ$  blowing angles, a significant portion of the high-energy fluid in the secondary flow merges into the low-energy fluid within the boundary layer, resulting in the nearly vanishing downstream separation zone at the blowing position. As

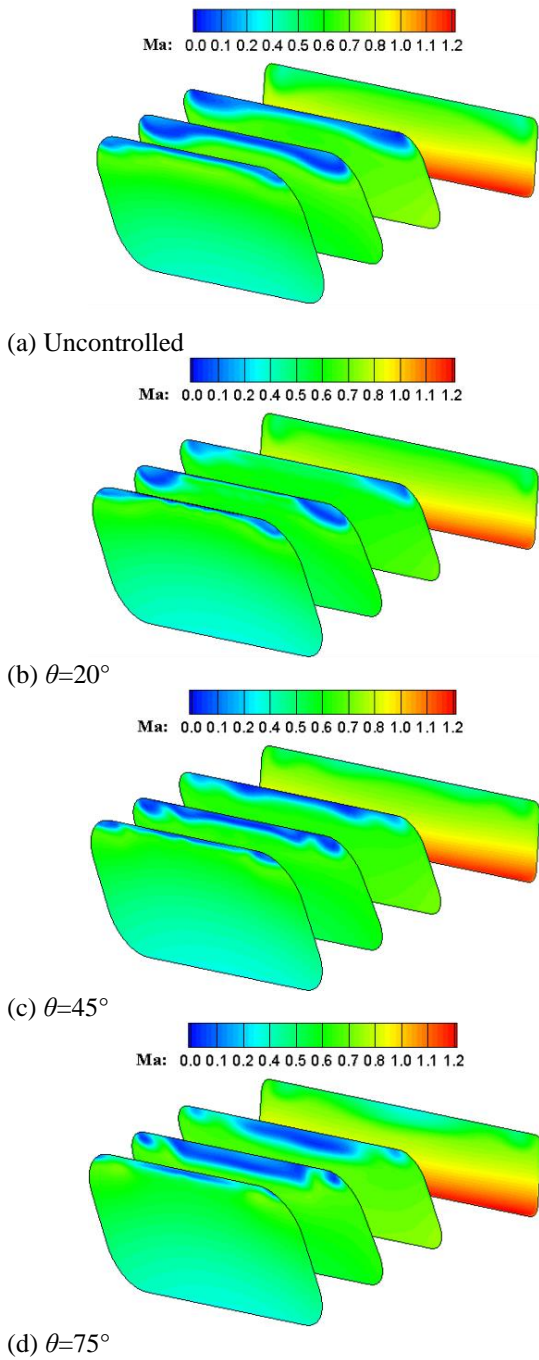
the downstream flow capacity increases, the upstream flow separation weakens or disappears due to the shallow jet depth of the secondary flow in the normal direction. However, at  $45^\circ$  and  $60^\circ$  blowing angles, while separation zones persist both upstream and downstream of the blowing position, they are smaller than those under uncontrolled conditions. Conversely, at  $75^\circ$  and  $90^\circ$  blowing angles, the separation area significantly expands both upstream and downstream of the blowing position, surpassing that under uncontrolled conditions. This occurs because only a minor fraction of high-energy fluid enters the boundary layer at larger blowing angles, with most of the fluid entering the primary flow of the nozzle, wherein the secondary flow's role primarily becomes the separation of the front and back areas of the separation zone, causing substantial disruption to the nozzle's main flow.

Figure 14 further delineates Ma number distribution along the cross-section near the separation zone under the aforementioned blowing conditions. Notably, at smaller blowing angles, the low-speed zone predominantly localizes along the nozzle's side wall, with the central low-speed zone essentially absent. Contrastingly, at larger blowing angles, the low-speed region shifts nearer to the nozzle's center, reducing the low-speed area along the side wall while expanding the overall low-speed region. Consequently, the dimensions—both normal and transverse—of the low-speed zone within the nozzle are smaller at smaller blowing angles.

### 3.2.3 Effect of the BPR

Examining the favorable blowing positions ( $x/L=0.28$  in the front of the separation zone and  $x/L=0.30$  in the separation zone) and blowing angles ( $\theta=20^\circ$  and  $\theta=30^\circ$ ), we studied the influence of the BPR on the blowing effect by modifying the inlet total pressure of the secondary flow. In Fig. 15, variations in the total pressure recovery coefficient and thrust coefficient of the nozzle outlet are depicted concerning the BPR at different blowing positions and angles. Notably, diverse aerodynamic performance parameters exhibit distinct trends with an increase in the BPR. As the BPR increases, the total pressure recovery coefficient consistently increases across different blowing positions and angles. This rise occurs due to a greater infusion of total pressure from the secondary flow, augmenting the total pressure recovery coefficient. At smaller blowing angles, most of the secondary flow mixes with low-energy fluid in the boundary layer, causing minimal interference with the main flow. With the increase in the total pressure of the secondary flow, the supplement of the total pressure of the nozzle increases, and the total pressure recovery coefficient increases.

However, the thrust coefficient behaves differently with increasing BPR at distinct blowing positions ( $x/L=0.28$  and  $x/L=0.30$ ). At  $x/L=0.28$ , the thrust coefficient initially ascends before declining, whereas at  $x/L=0.30$ , it experiences rapid growth followed by a slower increase. These divergent trends are attributed to varying jet depths resultant from different BPRs within a specific blowing duct configuration. An escalation in the BPR amplifies the secondary flow velocity at the blowing duct outlet, subsequently increasing the jet depth. This



**Fig. 14 Distributions of Ma number under different conditions**

eightened jet depth may disrupt the main flow of the nozzle. At a small BPR, the blown secondary fluid undergoes mixing with the low-energy fluid in the boundary layer because of the small jet depth, and the energy is injected into the latter. When the BPR continues to increase from 0.9 to 1, the jet depth further increases, the boundary layer at  $x/L=0.28$  is thin, and some secondary flows gradually undergo mixing with the main fluid of the nozzle, leading to obstruction of the upstream fluid and a decrease in the nozzle thrust coefficient at  $x/L=0.28$ . Conversely, at  $x/L=0.30$ , despite the thicker boundary layer, a further increase in the jet pressure ratio still results in slight enhancement of the nozzle thrust coefficient.

To investigate the impact of different BPRs on airflow pressure within the nozzle and its interaction with the main

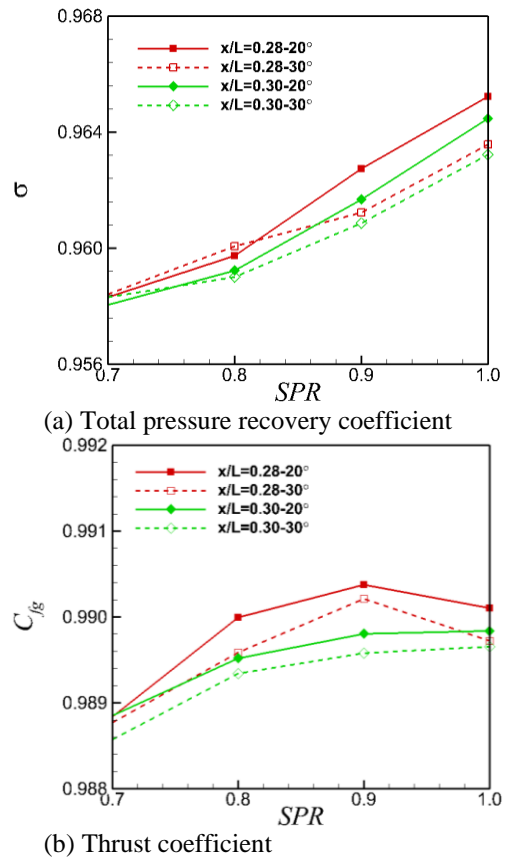


**Fig. 15 Variation in the aerodynamic parameters of nozzle outlet with the BPR at different blowing positions and blowing angles**

flow, Fig. 16 illustrates the distribution of relative static pressure at the symmetry plane. This occurs under uncontrolled conditions and at BPRs of 0.8, 0.9, and 1, respectively. Analysis reveals that the region influenced by blowing control primarily resides between the first and second bends, exerting minimal impact on airflow within the expansion section. Notably, a considerable pressure increase occurs near the blowing port when BPR is relatively low (0.8 and 0.9), resulting in an approximate 18% increase. However, this effect is negligible at other positions along the airflow. Upon reaching a BPR of 1, a significant pressure elevation beneath the blowing port is observed, signifying an increased jet depth and interference of the secondary flow with the nozzle's main flow. This indicates a limit to the blowing pressure, suggesting that excessively high pressure should be avoided.

In conclusion, enhancing the BPR improves the nozzle's aerodynamic performance, provided the secondary flow is not significantly mixed with the main flow. Excessive blowing pressure, however, can deteriorate nozzle performance. The optimal blowing scheme, determined by analyzing aerodynamic performance parameters and flow field characteristics, sets the blowing position at  $x/L=0.28$ , blowing angle at  $20^\circ$ , and BPR at  $BPR=0.9$ . This scheme boosts the thrust coefficient by 3.75% and the total pressure recovery coefficient by 0.52% compared with uncontrolled conditions.

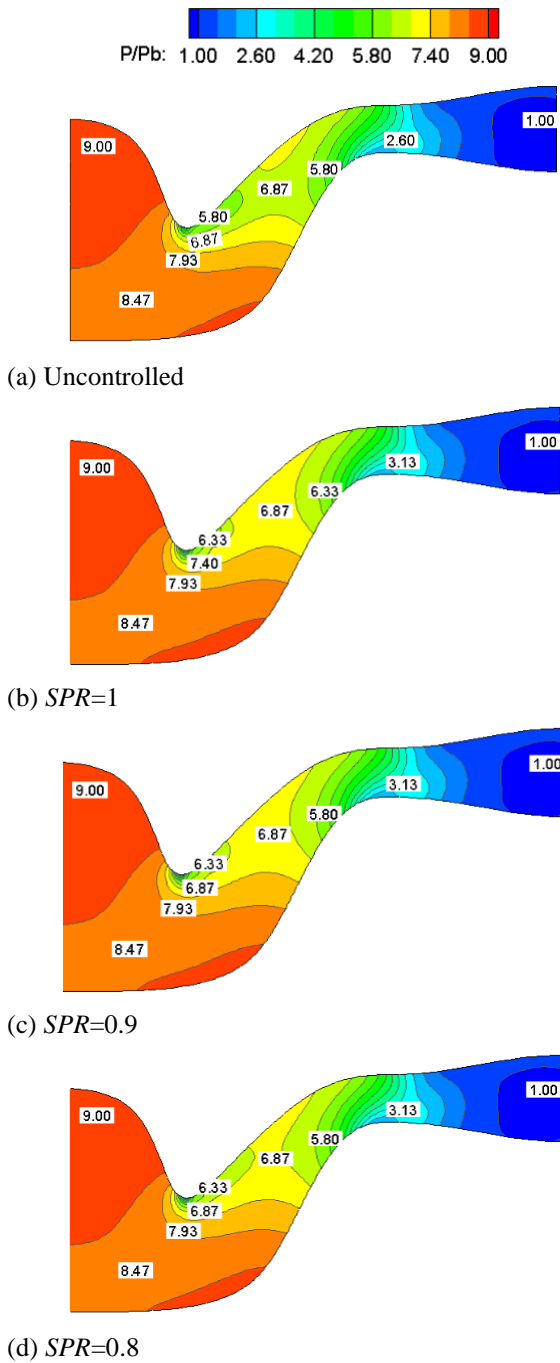


**Fig. 16 Distributions of static pressure under different conditions**

Figure 17a–h demonstrates the consistent existence of the reattachment phenomenon and the low-speed region near the side wall surface. This observation is depicted through the distribution of wall-limited streamlines and the Mach number on a longitudinal-section parallel to the nozzle's symmetry plane. Additionally, the figure illustrates the distribution of Mach numbers and streamlines at various span-wise positions under the blowing scheme. The parameter  $z/L$  denotes the ratio of the lateral coordinate of the longitudinal-section to the nozzle width ( $w$ ), with the blowing slot width approximately 0.4 times the width of the nozzle's longitudinal-section. Notably, the blowing control demonstrates minimal impact on the fluid outside the

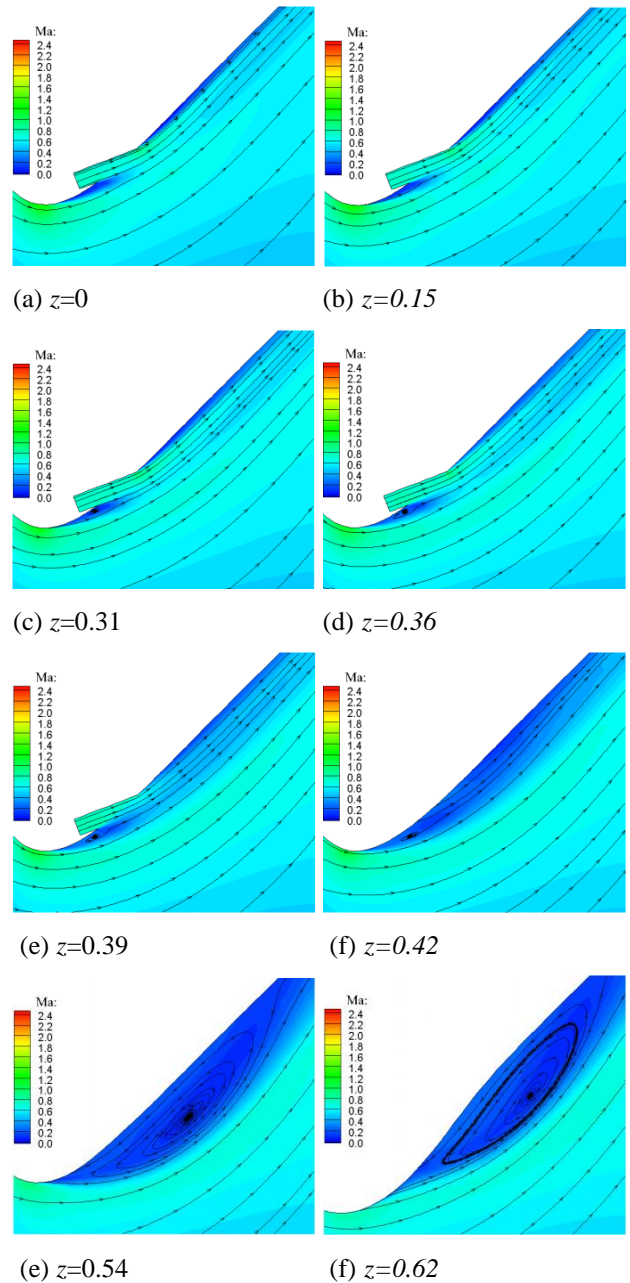


**Fig. 17 Distribution of Ma number and streamlines on the longitudinal-section parallel to the symmetry plane of the nozzle**

blowing groove, where the separation area persists. Fig. 17 (g) and (h) reveal a deliberate delay in the center of the separation area, with the separation center moving backward as it approaches the nozzle side wall. In the inner side of the blowing slot, the separation zone disappears, and the flow downstream of the first bend becomes smooth. However, when it is close to both ends of the blowing slot, as shown in Fig. 17 (d) and (e), the separation zone tends to form again.

#### 4. CONCLUSION

Addressing the flow separation phenomenon in the ultra-compact S-shaped convergent-divergent nozzle, this study employs blowing flow control through numerical simulation technology to mitigate flow separation and

enhance nozzle performance. The research delves into the effects of blowing position, BPR, and blowing angle on controlling flow separation. The key findings are as follows:

1) In the ultra-compact S-shaped convergent-divergent nozzle, flow separation occurs near the upper wall downstream of the first turn. Employing a blowing device near this separation zone allows high-energy fluid to enter the nozzle through the blowing groove, effectively mixing with low-energy fluid near the wall. This process supplements energy into the boundary layer, enhancing the low-energy fluid's ability to overcome adverse pressure gradients. The blowing position, blowing angle, and BPR significantly influence the size of the separation zone, emphasizing the importance of effectively mixing the injected secondary flow with low-energy wall-boundary fluid.

2) The blowing position exerts substantial influence on the flow field. Placing the blowing position ahead of the separation zone reduces the separation region before it but exhibits minimal effect on the flow field behind the blowing position. When the blowing position aligns with the separation zone and moves downstream, the separation region downstream gradually diminishes while the upstream separation region enlarges. The development of the downstream separation zone notably impacts nozzle aerodynamic performance compared to the upstream region. Consequently, blowing control within the separation zone proves more effective than control ahead of it.

3) Blowing angle significantly affects blowing control. A smaller blowing angle reduces the separation zone and enhances the aerodynamic performance of the ultra-compact S-shaped convergent-divergent nozzle. Conversely, an increased blowing angle augments secondary flow mixing with the main flow, hindering upstream fluid movement at the blowing point, forming an "aerodynamic wall," and subsequently deteriorating nozzle performance. A smaller blowing angle, around the middle of the separation zone ( $x/L=0.28$  and  $x/L=0.30$ ), causes the downstream flow separation phenomenon to nearly vanish.

4) Appropriate increases in BPR, under conditions ensuring well-mixed secondary flow with low-energy fluid without disturbing the main flow, improve the nozzle's aerodynamic performance by appropriately increasing the BPRs. Elevated BPRs increase jet depth, total pressure recovery coefficient, and initially enhance thrust coefficient before a subsequent decrease. Optimal blowing control occurs when the blowing position lies in the middle of the separation zone.  $BPR=0.9$  and  $\theta=20^\circ$  constitute the best schemes in this study, increasing total pressure recovery coefficient and thrust coefficient by approximately 0.52% and 3.75%, respectively, compared with the reference nozzle.

5) Reattachment phenomena and low-speed zones are observed near the side wall. Inside the blowing groove, the separation zone essentially disappears, resulting in smoother downstream flow after the initial bend. However, nearing the ends of the blowing groove, the

separation zone tends to redevelop. While blowing control has minimal effect on the fluid outside the blowing groove, it delays the center of the separation area appropriately. In comparison to suction control, blowing control offers a broader lateral control range. It does not eliminate lateral vortices but effectively weakens lateral flow.

## ACKNOWLEDGEMENTS

The authors would like to express their gratitude for the financial support of Science Center for Gas Turbine Project (No. P2022-B-II-010-001), the National Natural Science Foundation of China (Grant No. 52376032), the National Science and Technology Major Project (Grant No. J2019-II-0015-0036), and the Science Center for Gas Turbine Project (No. P2022-B-I-002-001).

## CONFLICT OF INTEREST

The author have no competing interests or conflicts to disclose.

## AUTHORS CONTRIBUTION

**J. W. Shi** and **Z. H. Hui**: methodology; formal analysis; writing-original draft; **L. Zhou** and **Z. X. Wang**: Writing-review & editing; Project administration. All authors have read and agreed to the published version of the manuscript.

## REFERENCES

- Chen, Z. J., & Wang, J. J. (2012). Numerical investigation on synthetic jet flow control inside an S-inlet duct. *Science China Technological Sciences*, 55, 2578–2584. <https://doi.org/10.1007/s11431-012-4970-y>
- Crowe, D. S., & Martin, C. L. (2015). *Hot streak characterization in serpentine exhaust nozzles*. Aiaa/sae/asee Joint Propulsion Conference.
- Crowe, D. S., & Martin, C. L. (2019). Hot streak characterization of high-performance double-serpentine exhaust nozzles at design conditions. *Journal of Propulsion and Power*, 35(3), 501–511. <https://doi.org/10.2514/1.B37235>
- He, P., & Dong, J. Z. (2015). Effect of slot orientation on synthetic jet-based separation control in a serpentine inlet. *Journal of Aerospace Power*, 30(2), 306–314. <https://doi.org/10.13224/j.cnki.jasp.2015.02.007>
- Hui, Z. H., Shi, J. W., Zhou, L., Wang, Z. X., & Liu, Y. Q. (2021) Experimental investigation of serpentine nozzles for turbofan. *Aerospace Science and Technology*, 117, 106892. <https://doi.org/10.1016/j.ast.2021.106892>
- Jing, J. P., & Guo, R. W. (2007). Experiment of boundary layer suction in serpentine inlet under ground running. *Journal of Nanjing University of Aeronautics and Astronautics*, 39(1), 30–36. <https://doi.org/10.3969/j.issn.1005-2615.2007.01.007>

- Kunik, W. G. (1986). *Application of a computational model for vortex generators in subsonic internal flows*. AIAA/ASME/SAE/ASEE 22nd Joint Propulsion Conference. Huntsville, Alabama.
- Liu, L. (2015). *Investigation of S shaped inlet distortion control and its impact on the flow field of the rear transonic fan-stage* [Ph. D. thesis, Harbin Institute of technology], Harbin, China.
- Reddy, N. K., & Sankar, M. (2020). Buoyant convective transport of nanofluids in a non-uniformly heated annulus. *Journal of Physics: Conference Series*, 1597, 012055. <https://doi.org/10.1088/1742-6596/1597/1/012055>
- Sang, Z. K. (2010). *Optimal design and active flow control of half flush-mounted S-duck inlet* [Master thesis, Harbin Institute of technology], Harbin, China.
- Sankar, M., Girish, N., & Siri, Z. (2018). Fully developed magnetoconvective heat transfer in vertical double-passage porous annuli. *Springer Transactions in Civil and Environmental Engineering*, 217–249. [https://doi.org/10.1007/978-981-10-8773-8\\_7](https://doi.org/10.1007/978-981-10-8773-8_7)
- Sankar, M., Kiran, S., Ramesh, G. K., & Makinde, O. D. (2017). Natural convection in a non-uniformly heated vertical annular cavity. *Defect and Diffusion Forum*, 377, 189–199. <https://doi.org/10.4028/www.scientific.net/DDF.377.189>
- Sankar, M., Pushpa, B. V., Prasanna, B. M. R., & Do, Y. (2016). Influences of size and location of a thin baffle on natural convection in a vertical annular enclosure. *Journal of Applied Fluid Mechanics*, 9, 2671–2684. <https://doi.org/10.29252/jafm.09.06.25501>
- Song, B. F., Feng, X. Q., & Hu, Y. (2010). The consideration of the next generation fighter under air and space combat environment. *Advances in Aeronautical Science and Engineering*, 1(2), 107–111. <https://doi.org/10.16615/j.cnki.1674-8190.2010.02.020>
- Sun, B. G., Li, F., & Qiu, Z. (2011). *Research on infrared radiation characteristics of binary nozzle jet*. National Conference on Optoelectronics and Quantum Electronics Technology, China.
- Sun, X. L., Wang, Z. X., & Zhou, L. (2014). Experimental and computational investigation of double serpentine nozzle. *Proceedings of the Institution of Mechanical Engineers, Part G: Journal of Aerospace Engineering*, 229(11), 2035–2050. <https://doi.org/10.1177/0954410014564402>
- Swamy, H. A. K., Sankar, M., & Reddy, N. K. (2022). Analysis of entropy generation and energy transport of cu-water nanoliquid in a tilted vertical porous annulus. *International Journal of Applied and Computational Mathematics*, 8, 1-10. <https://doi.org/10.1007/s40819-021-01207-y>
- Vakili, A. D., Wu J. M., & Liver P. (1985). *Flow control in a diffusing S-duct*. AIAA ShearFlow Control Conference, Boulder, Colorado
- Vikas, K., & Farrukh, A. (2003). *Use of supersonic microjets for active separation control in diffusers*. 33rd AIAA Fluid Dynamics Conference and Exhibit, Orlando, Florida.
- Wang, Z. X., Yu, M. Z., & Shi, J. W. (2018). The research on flow mechanism and flow control method of ultra-compact serpentine convergent divergent nozzle. *Journal of Engineering Thermophysics*, 39(8), 1718–1724. <https://doi.org/CNKI:SUN:GCRB.0.2018-08-012>
- Wise, K. A. (2023). *X-45 program overview and flight test status*. AIAA Unmanned Unlimited Systems, Technologies, and Operations. AIAA-2003-6645.
- Xu, D. G., Sang, J. H., & Luo, M. D. (2012). Research on application of UAV's infrared stealth technology. *Infrared and Laser Engineering*, 41(12), 3154–3159. <https://doi.org/10.3969/j.issn.1007-2276.2012.12.004>
- Zhao, Z. S., Dong, J., & Guo, C. P. (2010). Numerical simulation and optimization of inlet jet flow control. *Aerodynamic Research and Experiment*, 2, 1–8. <https://doi.org/10.13224/j.cnki.jasp.2010.02.017>
- Zhao, Z. S., Dong, J., & Guo, C. P. (2011). Parameters optimization of passive flow control device for a dual S inlet by numerical vortex generator model. *Acta Aerodynamica Sinica*, 29(1), 22–26. <https://doi.org/10.3969/j.issn.0258-1825.2011.01.004>
- Zhou, L., Meng, Y. B., & Wang, Z. X. (2021). Numerical study on flow characteristics of serpentine convergent divergent nozzle. *Journal of Propulsion Technology*, 42(1), 103–113. <https://doi.org/10.13675/j.cnki.tjjs.200271>